Pergamon

Int. J. Heat Mass Transfer. Vol. 41, No. 17, pp. 2619–2637, 1998

Printed in Great Britain
0017–9310/98 $19.00+0.00

PII: S0017–9310(97)00325–6

Analytical modeling of the startup characteristics of asymmetrical flat-plate and disk-shaped heat pipes

N. ZHU and K. VAFAI†

Department of Mechanical Engineering, The Ohio State University, Columbus, Ohio 43210, U.S.A.

(*Received* 14 *May* 1997 *and in final form* 8 *October* 1997)

Abstract—An analytical model is developed for the startup transient of asymmetrical flat-plate and disk-shaped heat pipes. The model solves the proper transient heat conduction equations for the heat pipe wall and liquid–wick regions. A quasi-steady state, pseudo three-dimensional approximation is used for the vapor transient behavior. The heat transfer within the wall and liquid–wick regions is coupled with the vapor phase at the liquid–vapor interfaces. Analytical solutions of temperature, vapor velocity, and vapor pressure distributions are obtained based on an in-depth integral method. Results covering the entire startup transient are presented for disk-shaped and flat-plate heat pipes. © 1998 Elsevier Science Ltd. All rights reserved.

INTRODUCTION

Asymmetrical flat-plate and disk-shaped heat pipes have some favorable features compared with conventional symmetrical heat pipes, such as geometry adaptation, ability for very localized heat dissipation and for producing an entirely isothermal surface. These characteristics have attracted significant attention in electronics cooling and space applications [1–6]. Understanding of the transient behavior of asymmetrical flat-plate and disk-shaped heat pipes is important for the startup phase of applications. In general, the analysis developed for conventional symmetrical heat pipes cannot be applied to asymmetrical heat pipes, nor can it account for the different design and geometrical features of the flat-plate and disk-shaped heat pipes. A literature survey revealed that the limited transient heat pipe models reported in the open literature are all for symmetrical heat pipes and an analysis for asymmetrical heat pipe startup process is not available.

Various transient models for different heat pipe startup stages have been developed [7–10]. All of these studies deal with the conventional cylindrical heat pipes. Almost all the transient heat pipe models reported in the literature are concentrated on a numerical simulation. This is because the analysis of heat pipe dynamics is quite complicated and a relevant analytical solution is difficult to obtain. Only a few analytical studies have been reported on the heat pipe frozen startup process such as those by Sockol and Forman [11] and Ochterbeck [12]. These works are based on the use of a lumped one-dimensional model. These analytical frozen startup models neglect temperature difference and heat transfer across heat pipe wall and wick and therefore cannot be applied to fully-thawed heat pipe startup process. For the startup of a fully-thawed heat pipe, the temperature difference across the heat pipe wall and liquid–wick is significant. While numerical models based on different simplifying assumptions have been developed, an analytical model for the startup process of a fully-thawed heat pipe is not available at present. An analytical model for the fully-thawed heat pipe can provide a quick prediction method for its transient operation and can aid in understanding the underlying physical phenomena.

It has been found that under normal conditions the transient response of a heat pipe is mainly determined by the thermal capacity and conductance of the heat pipe wall, wick, and working fluid and is only slightly influenced by liquid and vapor dynamics [7]. Following this finding, Chang and Colwell [7] analyzed heat pipe transient operation by solving the two-dimensional heat conduction equations for the heat pipe wall and the liquid saturated wick regions, which are thermally coupled to a lumped vapor model. The effect of liquid flow on the heat transfer is neglected by treating the liquid-saturated wick as a pure conducting medium with an effective thermal conductivity.

Bowman and Hitchcock [13] studied the transient vapor flow experimentally and numerically. Their results show that the vapor transient periods are very short and the vapor in the heat pipe can be accurately modeled using the steady-state governing equations. Based on their observation, Seo and El-Genk [9] developed a two-dimensional transient model for a liquid metal heat pipe which incorporates a quasi-

† Author to whom correspondence should be addressed. Tel.: 001 614 292 6560. Fax: 001 614 292 3163. E-mail: vafai.1@osu.edu.

NOMENCLATURE

C_P	specific heat [J kg^{-1} K^{-1}]
h	thickness [m]
h_{conv}	convective heat transfer coefficient [W m^{-2} K^{-1}]
h_{fg}	latent heat of working fluid [kJ kg^{-1}]
k	thermal conductivity [W m^{-1} K^{-1}]
L	length of the flat-plate heat pipe [m]
L_e	length of heat input zone of the flat-plate heat pipe [m]
$\dot{m}$	evaporation/condensation mass flux [kg m^{-2} s^{-1}]
p	pressure [Pa]
q_1	heat flux at the wall–wick interface [W m^{-2}]
q_{in}	input heat flux at the evaporator wall outer surface [W m^{-2}]
q_e	heat flux at the evaporator liquid–vapor interface [W m^{-2}]
q_c	heat flux at the condenser liquid–vapor interface [W m^{-2}]
r, y	radial and vertical coordinates used for the disk-shaped heat pipe [m]
R	radius of the disk-shaped heat pipe [m]
R_e	radius of the heat input zone of the disk-shaped heat pipe [m]
t	time [s]
T	temperature [K]
T_1	wall–wick interface temperature [K]
T_i	initial temperature [K]
T_∞	ambient temperature [K]
u, v	radial and vertical vapor velocity components [m s^{-1}]
$\mathbf{v}_1$	vapor injection velocity [m s^{-1}]
$\mathbf{v}_2$	vapor suction velocity [m s^{-1}]
x, y, z	coordinates used in the analysis of the flat-plate heat pipe [m].

Greek symbols

α	thermal diffusivity
δ	thermal layer length [m]
ε	porosity
η	alternative coordinate, $\eta = y - h_v$ or $\eta = -y$
θ	angular coordinate
μ	dynamic viscosity [m^2 s^{-1}]
ξ	alternative coordinate, $\xi = h_v + h_w + h_{wa} - y$
ρ	density [kg m^{-3}].

Subscripts

eff	effective value for the liquid–wick
l	liquid phase
lv	liquid–vapor interface
v	vapor phase
w	wick structure
wa	heat pipe wall.

steady state approximation for the vapor phase. Their model predictions agree well with the experimental results reported by Merrigan *et al.* [14].

In the present study, an analytical model is developed for the transient behavior of the fully thawed asymmetrical flat-plate and disk-shaped heat pipes during startup process. The heat transfer in the liquid-saturated wick is described using a heat conduction model, which is thermally coupled with a quasi-steady state pseudo-three-dimensional vapor model. Analytical solutions are obtained by solving the governing differential equations for the wall, the liquid-saturated wick and the vapor regions.

ANALYTICAL MODELING

The schematics of the asymmetrical disk-shaped and flat-plate heat pipes and the coordinate systems used in the study are shown in Figs. 1 and 2, respectively. Heat is primarily transported through the liquid-saturated wick by conduction in normal operation. Therefore, the effects of the liquid flow within the wick is neglected in our transient model. It should be noted that, while having a negligible influence on the temperature distribution in the heat pipe, the liquid flow is very important in the determination of the capillary limit of the heat pipe. The capillary limit is determined by using a comprehensive model for the liquid and vapor flow as established in [15] for the disk-shaped heat pipe and in [16] for the flat-plate heat pipe.

It has been determined that the effects of heat conduction along the heat pipe is negligible during transient operation of non-liquid metal heat pipes [17]. Based on this observation, the heat conduction along the heat pipe is neglected in the present study and a one-dimensional heat conduction model is used for the heat transfer within the heat pipe wall and liquid-saturated wick regions. The energy equation in the heat pipe wall region is

$$(\rho c_p)_{wa} \frac{\partial T_{wa}}{\partial t} = k_{wa} \frac{\partial^2 T_{wa}}{\partial y^2} \tag{1}$$

and in the top and bottom wick region is

$$(\rho c_p)_{eff} \frac{\partial T_l}{\partial t} = k_{eff} \frac{\partial^2 T_l}{\partial y^2} \tag{2}$$

where $(\rho c_p)_{eff} = \varepsilon_w \rho_l c_{pl} + (1-\varepsilon_w)(\rho c_p)_w$, ε_w is the porosity of the top and bottom wicks, and $(\rho c_p)_w$ is

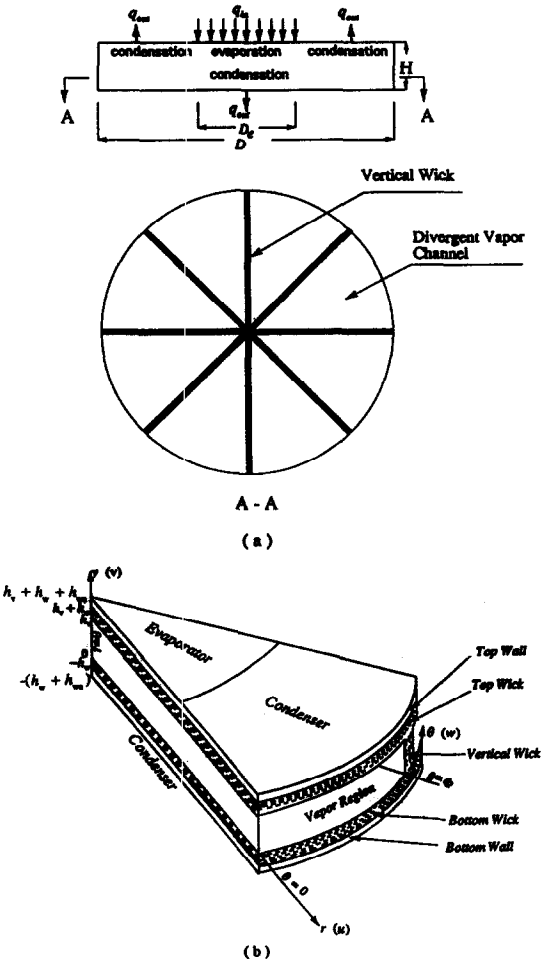

Fig. 1. Schematic of the disk-shaped heat pipe: (a) geometry of the heat pipe, (b) the coordinate system used in the analysis.

the heat capacity of the top and bottom wick structure material. The local volume averaging method is used here to obtaining equation (2). The effective thermal conductivity for the sintered wick is calculated using the equation given by Dunn and Reay [18]:

$$k_{\text{eff}} = k_{\text{w}}\left[\frac{2+k_{\text{l}}/k_{\text{w}}-2\varepsilon_{\text{w}}(1-k_{\text{l}}/k_{\text{w}})}{2+k_{\text{l}}/k_{\text{w}}+\varepsilon_{\text{w}}(1-k_{\text{l}}/k_{\text{w}})}\right]. \tag{3}$$

Since heat conduction along the heat pipe is neglected and a one-dimensional model is used for the heat transfer within the heat pipe and liquid-saturated wick regions, the analytical model for the heat transfer within the heat pipe wall and liquid-saturated wick regions are applicable to both asymmetrical flat-plate and disk-shaped heat pipes. However, for different type of heat pipes, different model for vapor phase is necessary. Due to the fact that the vapor transient periods are much smaller than the heat transfer time within the liquid saturated wick [9, 13], the vapor in the heat pipe can be accurately modeled using the steady state governing equations. Therefore, a quasi-steady state, pseudo-three-dimensional model is used for vapor in the present study. The governing equations for the vapor flow within the disk-shaped heat pipe are derived by Zhu and Vafai and presented in [19], which in the dimensional form are:

Mass Conservation Equation:

$$\frac{\partial u_{\text{v}}}{\partial r}+\frac{\partial \mathbf{v}_{\text{v}}}{\partial y}+\frac{u_{\text{v}}}{r}=0. \tag{4}$$

Momentum Conservation Equations:

$$\rho_{\text{v}}\left(u_{\text{v}}\frac{\partial u_{\text{v}}}{\partial r}+\mathbf{v}_{\text{v}}\frac{\partial u_{\text{v}}}{\partial y}\right)=-\frac{\partial p_{\text{v}}}{\partial r}+\mu_{\text{v}}\left(\frac{\partial^2 u_{\text{v}}}{\partial y^2}+\frac{1}{r^2}\frac{\partial^2 u_{\text{v}}}{\partial \theta^2}\right) \tag{5}$$

$$\frac{\partial p_{\text{v}}}{\partial y}=0 \tag{6}$$

$$\frac{\partial p_{\text{v}}}{\partial \theta}=0. \tag{7}$$

The governing equations for the vapor flow within the flat-plate heat pipe are derived by Zhu and Vafai and presented in [16], which in the dimensional form are:

Mass Conservation Equation:

$$\frac{\partial u_{\text{v}}}{\partial x}+\frac{\partial \mathbf{v}_{\text{v}}}{\partial y}=0. \tag{8}$$

Momentum Conservation Equations:

$$\rho_{\text{v}}\left(u_{\text{v}}\frac{\partial u_{\text{v}}}{\partial x}+\mathbf{v}_{\text{v}}\frac{\partial u_{\text{v}}}{\partial y}\right)=-\frac{\partial p_{\text{v}}}{\partial x}+\mu_{\text{v}}\left(\frac{\partial^2 u_{\text{v}}}{\partial y^2}+\frac{\partial^2 u_{\text{v}}}{\partial z^2}\right) \tag{9}$$

$$\frac{\partial p_{\text{v}}}{\partial y}=0 \tag{10}$$

$$\frac{\partial p_{\text{v}}}{\partial z}=0. \tag{11}$$

For a fully thawed low-temperature heat pipe, the vapor phase is assumed to be saturated, therefore there is no need to solve the energy equation for the vapor.

The boundary conditions at the heat pipe wall outer surfaces are given as:

Evaporator section:

At $y=h_{\text{v}}+h_{\text{w}}+h_{\text{wa}}$, $0\leqslant r\leqslant R_e$ (or $0\leqslant x\leqslant L_e$ for the flat-plate heat pipe)

$$k_{\text{wa}}\left.\frac{\partial T_{\text{wa}}}{\partial y}\right|_{y=h_{\text{v}}+h_{\text{w}}+h_{\text{wa}}}=q_{\text{in}}. \tag{12}$$

Condenser section:

At the upper condenser outer wall surface, i.e. $y=h_{\text{v}}+h_{\text{w}}+h_{\text{wa}}$, $R_e\leqslant r\leqslant R$ (or $L_e\leqslant x\leqslant L$ for the flat-plate heat pipe)

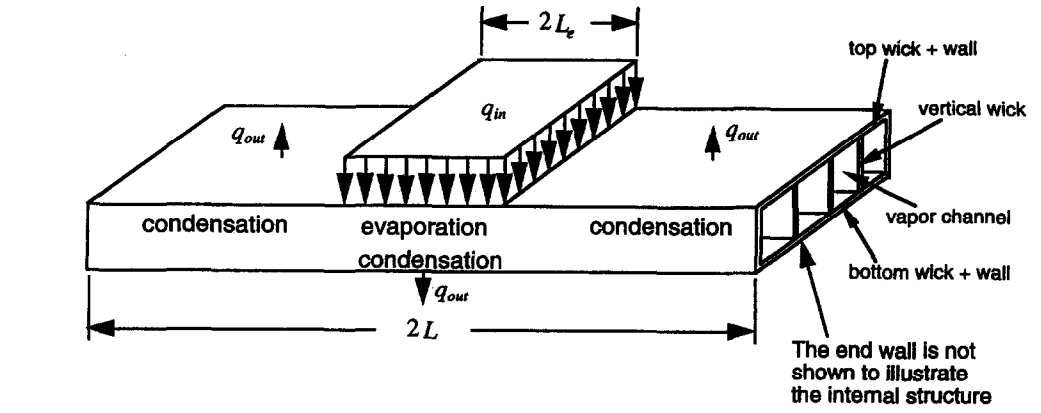

(a)

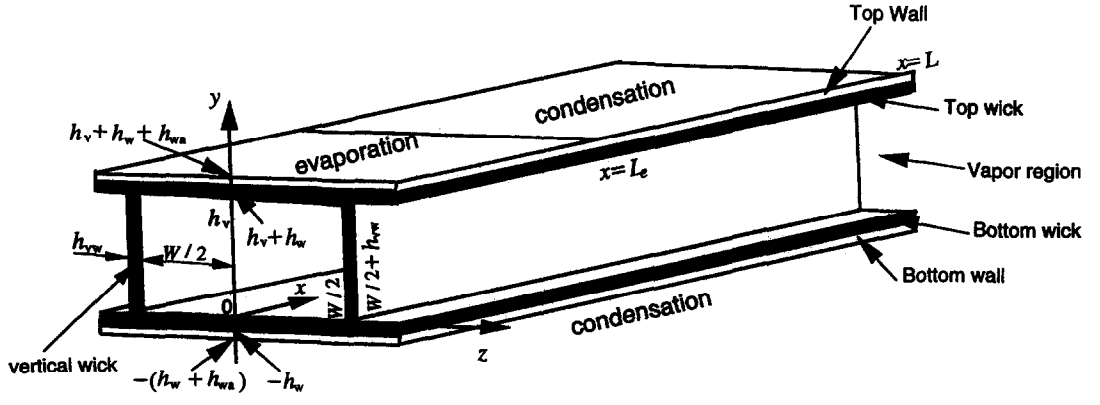

(b)

Fig. 2. Schematic of the flat-plate heat pipe: (a) geometry of the heat pipe, (b) the coordinate system used in the analysis.

$$-k_{wa}\left.\frac{\partial T_{wa}}{\partial y}\right|_{y=h_v+h_w+h_{wa}} = h_{conv}(T_{wa}(y=h_v+h_w+h_{wa},t)-T_\infty). \quad (13)$$

At the lower condenser outer wall surface, i.e. $y=-(h_w+h_{wa})$, $0\leqslant r\leqslant R$ (or $0\leqslant x\leqslant L$ for the flat-plate heat pipe)

$$k_{wa}\left.\frac{\partial T_{wa}}{\partial y}\right|_{y=-(h_w+h_{wa})} = h_{conv}(T_{wa}(y=-h_w-h_{wa},t)-T_\infty) \quad (14)$$

where h_{conv} is the convective heat transfer coefficient, T_∞ is the coolant temperature.

The boundary condition at the wall–wick interfaces ($y=h_v+h_w$ and $y=-h_w$) are:

$$T_{wa}(y=h_v+h_w,t)=T_l(y=h_v+h_w,t),$$
$$T_{wa}(y=-h_w,t)=T_l(y=-h_w,t) \quad (15)$$

$$k_{wa}\left.\frac{\partial T_{wa}}{\partial y}\right|_{y=h_v+h_w} = k_w\left.\frac{\partial T_l}{\partial y}\right|_{y=h_v+hf_w},$$
$$k_{wa}\left.\frac{\partial T_{wa}}{\partial y}\right|_{y=-h_w} = k_w\left.\frac{\partial T_l}{\partial y}\right|_{y=-h_w}. \quad (16)$$

At the liquid–vapor interfaces ($y=0$ and $y=h_v$), the continuity of temperature field requires

$$T_v(y=0,t)=T_l(y=0,t),$$
$$T_v(y=h_v,t)=T_l(y=h_v,t). \quad (17)$$

The energy balance at the liquid–vapor interfaces yields

$$k_w\left.\frac{\partial T_l}{\partial y}\right|_{y=h_v} = k_v\left.\frac{\partial T_v}{\partial y}\right|_{y=h_v}+\dot{m}h_{fg},$$
$$k_w\left.\frac{\partial T_l}{\partial y}\right|_{y=0} = k_v\left.\frac{\partial T_v}{\partial y}\right|_{y=0}+\dot{m}h_{fg} \quad (18)$$

where $\dot{m}$ is the evaporation/condensation mass fluxes. For evaporation,

$$\dot{m} = \rho_v v_1. \tag{19}$$

For condensation,

$$\dot{m} = \begin{cases} -\rho_v v_2, & y = h_v \\ \rho_v v_2, & y = 0 \end{cases}. \tag{20}$$

For the vapor velocity component u, based on the results established in [15], the non-slip boundary condition is applied at the liquid–vapor interfaces as well as the evaporator and condenser ends.

The initial condition is

$$T_{wa} = T_l = T_v = T_i \quad \text{at } t = 0. \tag{21}$$

Since both the temperature and the heat flux at the liquid–vapor interfaces are unknown, a marching scheme is used for time. For the quasi-steady state vapor model employed in the analysis, at each time step, the energy entering the vapor phase within the evaporator section should equal to that rejected from the vapor phase within the condenser section. This energy balance for the vapor phase at each time step, along with the above governing equations and boundary conditions, provides the necessary relations for obtaining a closed mathematical solution.

ANALYTICAL SOLUTION

Evaporator wall and wick regions

The heat conduction equations (1) and (2) for the temperature field within the heat pipe wall and the liquid-saturated wick regions are integrated with respect to y from the heat pipe wall outer surface to a distance $\delta_e(t)$, beyond which the initial temperature distribution remains unaffected by the applied heat load. When this thermal layer reaches the liquid–vapor interface, the heat conduction equations are integrated over the entire wall and liquid–wick regions and the boundary conditions (17) and (18) are applied.

To facilitate the derivation of the temperature distributions, an alternative coordinate, $\xi = h_v + h_w + h_{wa} - y$, is employed (Fig. 3(a)). The energy equations (1) and (2) in the ξ-coordinate system reduce to

$$(\rho c_p)_{wa} \frac{\partial T_{wa}}{\partial t} = k_{wa} \frac{\partial^2 T_{wa}}{\partial \xi^2}, \quad \text{for } 0 \leqslant \xi \leqslant h_{wa}, \quad t \geqslant 0 \tag{22}$$

$$(\varepsilon c_p)_{eff} \frac{\partial T_l}{\partial t} = k_{eff} \frac{\partial^2 T_l}{\partial \xi^2}$$

$$\text{for } h_{wa} \leqslant \xi \leqslant h_{wa} + h_w, \quad t \geqslant 0. \tag{23}$$

The temperature distribution is approximated by using a second order polynomial in ξ, that is:

$$T(\xi, t) = a_0(t) + a_1(t)\xi + a_2(t)\xi^2. \tag{24}$$

For conduction problems, a comparison of approximate temperature distributions based on a second, third- and fourth-order polynomial approximation with exact solution shows that the simple second order polynomial approximation can yield reasonably good results which are sufficiently accurate for most engineering applications [20].

The analysis for the transient heat transfer within the evaporator wall and wick regions is divided into three stages. At $t = 0$, the heat load is applied to the evaporator wall outer surface and the thermal layer starts to develop. Before the thermal layer reaches the wall–wick interface, i.e. $\delta_e(t) \leqslant h_{wa}$, all the input heat is stored within the wall region hence resulting in the temperature increase within the wall region. The temperature field within the wick region and the vapor region remains unaffected. After the thermal layer reaches the wall–wick interface, the temperature gradients start to build up within the wick region, while the temperatures within the wall region keeps on rising. When the thermal layer reaches the liquid–vapor interface, the liquid at the liquid–vapor interface starts to evaporate. Part of the input heat is transported to the condenser section in the form of latent heat, while the other part of input heat is stored in the wall and wick regions to continue the temperature rise within these regions. The amount of the heat which is transported to the condenser section increases gradually and eventually equals to the amount of the input heat load under steady-state conditions.

(1) For the time period during which $\delta_e(t) \leqslant h_{wa}$

During this period, the boundary conditions are

$$-k_{wa} \left.\frac{\partial T_{wa}}{\partial \xi}\right|_{\xi=0} = q_{in}$$

$$T_{wa}(\xi = \delta_e(t), t) = T_i$$

$$\left.\frac{\partial T_{wa}}{\partial \xi}\right|_{\xi=\delta_e(t)} = 0. \tag{25}$$

Applying the boundary conditions given in equation (25) to equation (24) yields the temperature distribution:

$$T_{wa}(\xi, t) = T_i + \frac{q_{in}\delta_e(t)}{2k_{wa}} \left(1 - \frac{\xi}{\delta_e(t)}\right)^2 \quad 0 \leqslant \xi \leqslant \delta_e(t). \tag{26}$$

Substituting the temperature distribution given by equation (26) and the boundary conditions given by equation (25) into the integrated form [integrated with respect to ξ from 0 to $\delta_e(t)$] of equation (22) yields:

$$\delta_e(t) = \sqrt{6\alpha_{wa} t} \tag{27}$$

where $\alpha_{wa} = k_{wa}/(\rho c_p)_{wa}$ is the thermal diffusivity of the wall. The initial condition $\delta_e(t) = 0$ is used in obtaining equation (27).

The temperature distribution is then given by equa-

tions (26) and (27). The time for the thermal layer to reach the wall–wick interface is given by:

$$t_1 = \frac{h_{wa}^2}{6\alpha_{wa}}. \tag{28}$$

(2) For the time period during which $h_{wa} \leqslant \delta_e^*(t) \leqslant h_{wa} + h_w$

During this period, the boundary conditions for the wall region are:

$$-k_{wa}\left.\frac{\partial T_{wa}}{\partial \xi}\right|_{\xi=0} = q_{in}$$

$$T_{wa}(\xi = h_{wa}, t) = T_{1,e}(t)$$

$$-k_{wa}\left.\frac{\partial T_{wa}}{\partial \xi}\right|_{\xi=h_{wa}} = q_{1,e}(t) \tag{29}$$

and for the liquid saturated wick region are

$$T_l(\xi = h_{wa}, t) = T_{1,e}(t)$$

$$T_l(\xi = \delta_e^*(t), t) = T_i$$

$$\left.\frac{\partial T_l}{\partial \xi}\right|_{\xi=\delta_e^*(t)} = 0 \tag{30}$$

where $T_{1,e}(t)$ and $q_{1,e}(t)$ are the temperature and heat flux at the wall–wick interface in the evaporator section, respectively. It should be noted here that δ_e and δ_e^* are referring to the same thermal layer but in different regions and as such different expressions.

Applying the boundary conditions given by equation (29) to equation (24) yields the temperature distribution for the wall region

$$T_{wa}(\xi, t) = T_{1,e}(t) + \frac{q_{in}}{2\lambda_{wa}}\left(1 - \frac{\xi}{h_{wa}}\right)^2 + \frac{q_{1,e}(t)}{2\lambda_{wa}}\left[1 - \left(\frac{\xi}{h_{wa}}\right)^2\right],$$

$$0 \leqslant \xi \leqslant h_{wa}, \quad t_1 \leqslant t \leqslant t_2 \tag{31}$$

and applying the boundary conditions given by equation (30) to equation (24) yields the temperature distribution for the liquid-saturated wick region

$$\frac{T_l(\xi, t) - T_i}{T_{1,e}(t) - T_i} = \left(1 - \frac{\xi - h_{wa}}{\delta_e^*(t) - h_{wa}}\right)^2,$$

$$h_{wa} \leqslant \xi \leqslant \delta_e^*(t), \quad t_1 \leqslant t \leqslant t_2 \tag{32}$$

where $\lambda_{wa} = k_{wa}/h_{wa}$, and t_2 is the time for the thermal layer to reach the liquid–vapor interface. The continuity of heat flux at the wall–wick interface, equation (16), requires

$$T_{1,e}(t) = T_i + \frac{q_{1,e}(t)}{2k_{eff}}(\delta_e^*(t) - h_{wa}). \tag{33}$$

The two unknowns $\delta_e^*(t)$ and $q_{1,e}(t)$ are obtained by integrating the energy equations (22) and (23). Integrating equation (23) with respect to ξ from h_{wa} to $\delta_e^*(t)$ and utilizing the boundary conditions given by equation (30) and the temperature distribution given by equation (32) yields:

$$(T_{1,e}(t) - T_i)\frac{d\delta_e^*(t)}{dt} + (\delta_e^*(t) - h_{wa})\frac{dT_{1,e}(t)}{dt} = \frac{6\alpha_{eff}(T_{1,e}(t) - T_i)}{\delta_e^*(t) - h_{wa}} \tag{34}$$

where $\alpha_{eff} = k_{eff}/(\rho c_p)_{eff}$ is the effective diffusivity of the liquid-saturated wick. Utilizing the energy equation (23) to represent $dT_{1,e}(t)/dt$ in terms of the second spatial derivative of the temperature distribution given by equations (26) and (27) yields:

$$\delta_e^*(t) = h_{wa} + \sqrt{8\alpha_{eff}(t - t_1)}. \tag{35}$$

The initial condition $\delta_e^*(t_1) = h_{wa}$ is used to obtain equation (35). The time for the thermal layer to reach the liquid–vapor interface is obtained as:

$$t_2 = t_1 + \frac{h_w^2}{8\alpha_{eff}}. \tag{36}$$

Integrating equation (22) with respect to ξ from 0 to h_{wa} and utilizing the boundary conditions given by equation (29), the temperature distribution given by equation (31), and equations (33) and (34) yields:

$$q_{1,e}(t) = \frac{q_{in}}{A(t)}(t - t_1) \tag{37}$$

where

$$A(t) = \frac{(\delta_e^*(t) - h_{wa})^2}{6\alpha_{eff}} + \frac{k_{wa}h_{wa}}{2k_{eff}\alpha_{wa}}(\delta_e^*(t) - h_{wa}) + \frac{k_{wa}^2}{3\alpha_{wa}}. \tag{38}$$

The initial conditions $\delta_e^*(t) = h_{wa}$ and $q_{1,e}(t_1) = 0$ are used to obtain equation (37). The temperature distributions for the time period $t_1 \leqslant t \leqslant t_2$ are then given by equations (31)–(35) and (37).

(3) After thermal layer reaches the liquid–vapor interface

At $t = t_2$, the thermal layer reaches the liquid–vapor interface. The temperatures within the wall and the liquid-saturated wick regions still increase for $t > t_2$, while evaporation takes place at the liquid–vapor interface. Since the temperature variations within the vapor phase is negligible for low-temperature heat pipes [6, 17], the second term on the right hand side of equation (18) is negligible. Therefore, the vapor temperature is assumed to be equal to the liquid–vapor interface temperature and all the heat transferred to the liquid–vapor interface causes the change of phase and is subsequently transported by the vapor to the condenser section in the form of latent heat. Due to the fact that the vapor transient periods are very short compared to the response time within the liquid-saturated wick, a quasi-steady state model is employed in the present analysis for the vapor phase. This indicates that at any time, the heat transfer into

the vapor phase within the evaporator section equals to that rejected from the vapor phase within the condenser section.

When $t > t_2$, the boundary conditions for the wall region are the same as those specified in equation (29), while for the wick region they are

$$T_1(\xi = h_{wa}, t) = T_{1,e}(t)$$
$$-k_{eff}\frac{\partial T_1}{\partial \xi}\bigg|_{\xi=h_{wa}} = q_{1,e}(t)$$
$$T_1(\xi = h_{wa}+h_w, t) = T_{lv}(t) \quad (39)$$

where $T_{lv}(t)$ denotes the temperature at the liquid–vapor interface. Applying the boundary conditions given by equations (29) and (39) to equation (24) yields the temperature distribution for the wall region

$$T_{wa}(\xi, t) = T_{1,e}(t)+\frac{q_{in}}{2\lambda_{wa}}\left(1-\frac{\xi}{h_{wa}}\right)^2 + \frac{q_{1,e}(t)}{2\lambda_{wa}}\left[1-\left(\frac{\xi}{h_{wa}}\right)^2\right], \quad 0 \leqslant \xi \leqslant h_{wa}, \quad t \geqslant t_2 \quad (40)$$

which is the same as that given in equation (31), and for the wick region

$$T_1(\xi, t) = T_{lv}(t)-(T_{lv}(t)-T_{1,e}(t))\left[1-\left(\frac{\xi-h_{wa}}{h_w}\right)^2\right] - \frac{q_{1,e}(t)}{\lambda_{eff}}\frac{\xi-h_{wa}}{h_w}\left(1-\frac{\xi-h_{wa}}{h_w}\right), \quad h_{wa} \leqslant \xi \leqslant h_{wa}+h_w, \quad t \geqslant t_2 \quad (41)$$

where $\lambda_{eff} = k_{eff}/h_w$.

The two unknowns $T_{1,e}(t)$ and $q_{1,e}(t)$ are determined by integrating the energy equations (22) and (23) over the wall region and the wick region, respectively. Utilizing the temperature distributions given by equations (40) and (41) and solving the integrated equations for $T_{1,e}(t)$ and $q_{1,e}(t)$ yields:

$$\frac{dq_{1,e}(t)}{dt} = \left\{\frac{dT_{lv}(t)}{dt}-\left(\frac{2\alpha_{wa}}{k_{wa}h_{wa}} + \frac{6\alpha_{eff}}{k_{eff}h_w}\right)q_{1,e}(t)+\frac{6\alpha_{eff}}{h_w^2}(T_{1,e}(t)-T_{lv}(t))+\frac{2\alpha_{wa}}{k_{wa}h_{wa}}q_{in}\right\}\Bigg/\left(\frac{2}{3\lambda_{wa}}+\frac{1}{2\lambda_w}\right) \quad (42)$$

and

$$\frac{dT_{1,e}(t)}{dt} = \frac{1}{3\lambda_{wa}+4\lambda_{eff}} \times\left\{3\left(\frac{4\alpha_{eff}}{h_w^2}-\frac{\alpha_{wa}}{h_{wa}^2}\right)q_{1,e}(t)+\frac{3\alpha_{wa}}{h_{wa}^2}q_{in} - 2\lambda_{eff}\left[\frac{dT_{lv}(t)}{dt}+\frac{6\alpha_{eff}}{h_w^2}(T_{1,e}(t)-T_{lv}(t))\right]\right\}. \quad (43)$$

The heat flux at the liquid–vapor interface is then obtained as:

$$q_{lv,e}(t) = \frac{2k_{eff}}{h_w}[T_{1,e}(t)-T_{lv}(t)]-q_{1,e}(t). \quad (44)$$

Condenser wall and wick regions

As shown in the previous section, starting at $t = t_2$, a heat flux $q_{lv,c}(t)$ is applied to the liquid–vapor interface in the condenser section as a result of vapor condensation. The thermal layer develops from the liquid–vapor interface towards the heat pipe wall outer surface. To facilitate the derivation of the formulation, an alternative coordinate $\eta = y-h_v$ is employed for the top wall and wick regions of the condenser section, and $\eta = -y$ is employed for the bottom wall and wick regions (Fig. 3(b)). The energy equations (1) and (2) are then reduced to:

$$(\rho c_p)_{wa}\frac{\partial T_{wa}}{\partial t} = k_{wa}\frac{\partial^2 T_{wa}}{\partial \eta^2}, \quad \text{for } h_w \leqslant \eta \leqslant h_w+h_{wa}, \quad t \geqslant t_2 \quad (45)$$

$$(\rho c_p)_{eff}\frac{\partial T_1}{\partial t} = k_{eff}\frac{\partial^2 T_1}{\partial \eta^2} \quad \text{for } 0 \leqslant \eta \leqslant h_w, \quad t \geqslant t_2. \quad (46)$$

The analysis for the transient heat transfer within the condenser wall and wick regions is also divided into three stages: (1) before the thermal layer reaches the wall–wick interface, (2) the time after the thermal layer reaches the wall–wick interface until the time when the thermal layer reaches the wall outer surface, and (3) after the thermal layer reaches the wall outer surface. Based on prior discussion, the temperature distribution is approximated by using a second order polynomial:

$$T(\eta, t) = a_0(t)+a_1(t)\eta+a_2(t)\eta^2. \quad (47)$$

(1) For the time period during which $\delta_c(t) \leqslant h_w$

During this period, the boundary conditions are:

$$T_1(\eta = 0, t) = T_{lv}(t)$$
$$T_1(\eta = \delta_c(t), t) = T_i$$
$$\frac{\partial T_1}{\partial \eta}\bigg|_{\eta=\delta_c(t)} = 0. \quad (48)$$

Applying the boundary conditions given by equation (48) in equation (47) yields the following temperature distribution:

$$\frac{T_1(\eta, t)-T_i}{T_{lv}(\eta, t)-T_i} = \left(1-\frac{\eta}{\delta_c(t)}\right)^2, \quad 0 \leqslant \eta \leqslant \delta_c(t), \quad t \geqslant t_2. \quad (49)$$

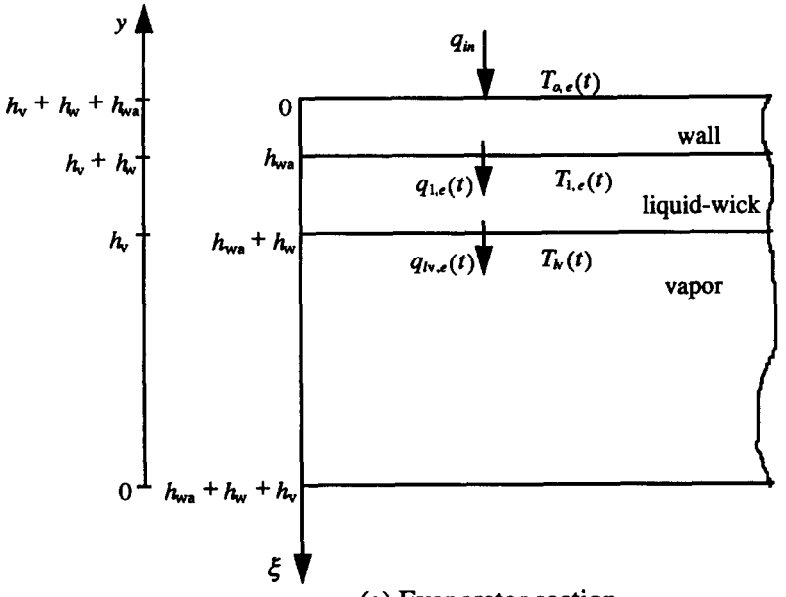

(a) Evaporator section

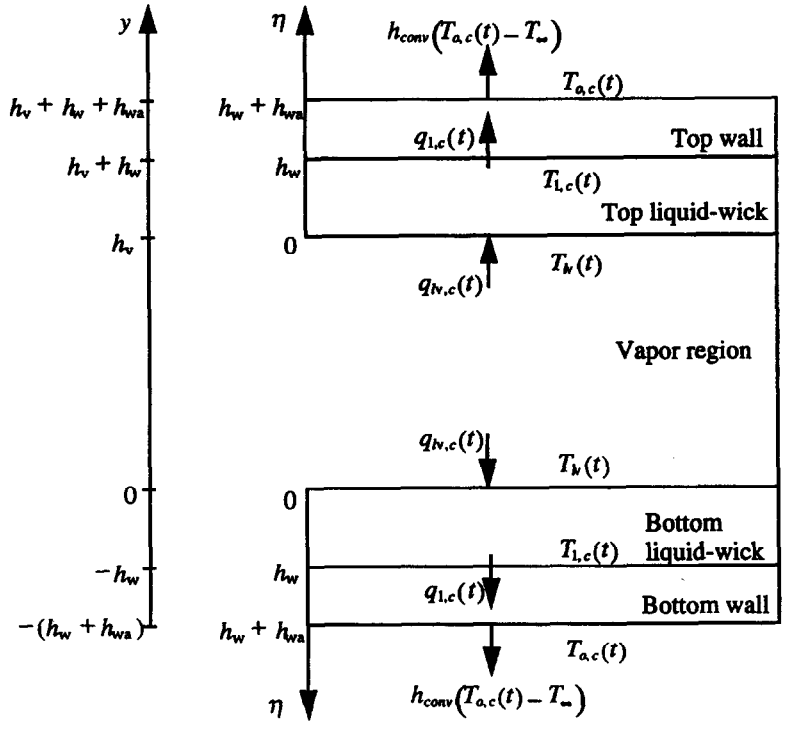

(b) Condenser section

Fig. 3. The alternative coordinate systems used in the analysis.

Integrating the energy equation (46) with respect to η from 0 to $\delta_c(t)$ and utilizing equation (49) yields:

$$\delta_c(t) = \sqrt{8\alpha_{\text{eff}}(t-t_2)}. \tag{50}$$

The initial condition $\delta_c(t = t_2) = 0$ is used to obtain equation (50). The time at which the thermal layer reaches the wall–wick interface is:

$$t_3 = t_2 + \frac{h_w^2}{8\alpha_{\text{eff}}}. \tag{51}$$

The heat flux at the liquid–vapor interface is therefore obtained as:

$$q_{\text{lv},c}(t) = \frac{2k_{\text{eff}}(T_{\text{lv}}(t)-T_i)}{\sqrt{8\alpha_{\text{eff}}(t-t_2)}}, \quad t_2 \leqslant t \leqslant t_3. \tag{52}$$

(2) For the time period during which $h_w \leqslant \delta_c^*(t) \leqslant h_w + h_{wa}$

During this period, the boundary condition for the wick region are:

$$T_1(\eta = 0, t) = T_{\text{lv}}(t)$$
$$T_1(\eta = h_w, t) = T_{1,c}(t)$$
$$-k_{\text{eff}}\frac{\partial T_1}{\partial \eta}\bigg|_{\eta=h_w} = q_{1,c}(t) \tag{53}$$

and for the wall region are

$$T_{wa}(\eta = h_w, t) = T_{1,c}(t)$$
$$T_{wa}(\eta = \delta_c^*(t), t) = T_i$$
$$\frac{\partial T_{wa}}{\partial \eta}\bigg|_{\eta=\delta_c^*(t)} = 0. \tag{54}$$

Utilizing the boundary conditions given by equation (53) in equation (47) yields the temperature distribution for the liquid-saturated wick region:

$$T_1(\eta, t) = T_{1,c}(t) + (T_{\text{lv}}(t) - T_{1,c}(t))\left(1-\frac{\eta}{h_w}\right)^2 + \frac{q_{1,c}(t)}{\lambda_{\text{eff}}}\frac{\eta}{h_w}\left(1-\frac{\eta}{h_w}\right), \quad 0 \leqslant \eta \leqslant h_w, \quad t \geqslant t_3. \tag{55}$$

Using the boundary conditions given by equation (54) to equation (47) yields the temperature distribution for the wall region:

$$\frac{T_{wa}(\eta, t) - T_i}{T_{1,c}(t) - T_i} = \left(1 - \frac{\eta - h_w}{\delta_c^*(t) - h_w}\right)^2, \quad h_w \leqslant \eta \leqslant \delta_c^*(t), \quad t \geqslant t_3. \tag{56}$$

The continuity of heat flux at the wall–wick interface yields:

$$T_{1,c}(t) = T_i + \frac{q_{1,c}(t)}{2k_{wa}}(\delta_c^*(t) - k_w). \tag{57}$$

Integrating the energy equation (45) with respect to η from h_w to $\delta_c^*(t)$ and utilizing equation (56) yields:

$$\delta_c^*(t) = h_w + \sqrt{8\alpha_{wa}(t-t_3)}. \tag{58}$$

The initial condition $\delta_c^*(t = t_3) = h_w$ is used to obtain equation (58). The time for the thermal layer to reach the wall outer surface is therefore given by:

$$t_4 = t_3 + \frac{h_{wa}^2}{8\alpha_{wa}}. \tag{59}$$

Integrating the energy equation (46) with respect to η from 0 to h_w and utilizing equations (55), (57) and (58) yields:

$$\frac{dq_{1,c}(t)}{dt} = -\frac{16\alpha_{\text{eff}}}{h_w^2}\left[\left(1 + \frac{k_{\text{eff}}}{k_{wa}h_w}\sqrt{2\alpha_{wa}(t-t_3)}\right)q_{1,c}(t) - \frac{k_{\text{eff}}}{h_w}(T_{\text{lv}}(t) - T_i)\right]. \tag{60}$$

The temperature distributions for the time period $t_3 \leqslant t \leqslant t_4$ are given by equations (55)–(58) and (60). The heat flux at the liquid–vapor interface during this time period is:

$$q_{\text{lv},c}(t) = \frac{2k_{\text{eff}}}{h_w}(T_{\text{lv}}(t) - T_i) - \left(1 + \frac{k_{\text{eff}}}{k_{wa}}\sqrt{\frac{8\alpha_{wa}}{h_w^2}(t-t_3)}\right)q_{1,c}(t). \tag{61}$$

(3) After the thermal layer reaches the wall outer surface

When $t \geqslant t_4$, part of the heat is conducted to the wall outer surface and dissipated by convection. During this time period, the boundary conditions for the wick region are the same as those specified in equation (53), while for the wall region they are

$$-k_{wa}\frac{\partial T_{wa}}{\partial \eta}\bigg|_{\eta=h_w+h_{wa}} = h_{\text{conv}}(T_{wa}(\eta = h_w + h_{wa}, t) - T_\infty)$$
$$T_{wa}(\eta = h_w, t) = T_{1,c}(t)$$
$$-k_{wa}\frac{\partial T_{wa}}{\partial \eta}\bigg|_{\eta=h_w} = q_{1,c}(t). \tag{62}$$

Applying boundary conditions given by equations (53) and (62) to equation (47) yields the temperature distribution for the wick region

$$T_1(\eta, t) = T_{1,c}(t) + (T_{\text{lv}}(t) - T_{1,c}(t))\left(1-\frac{\eta}{h_w}\right)^2 + \frac{q_{1,c}(t)}{\lambda_{\text{eff}}}\frac{\eta}{h_w}\left(1-\frac{\eta}{h_w}\right), \quad 0 \leqslant \eta \leqslant h_w, \quad t \geqslant t_4 \tag{63}$$

and for the wall region:

$$T_{wa}(\eta, t) = T_{1,c}(t) - \frac{q_{1,c}(t)}{k_{wa}}(\eta - h_w) + \left(\frac{1+Bi_{wa}}{2+Bi_{wa}}\frac{q_{1,c}(t)}{k_{wa}h_{wa}} - \frac{Bi_{wa}}{2+Bi_{wa}}\frac{T_{1,c}(t)-T_\infty}{h_{wa}^2}\right)(\eta - h_w)^2, \quad h_w \leqslant \eta \leqslant h_w + h_{wa}, \quad t \geqslant t_4 \tag{64}$$

where $Bi_{wa} = h_{conv}h_{wa}/k_{wa}$.

Integrating the energy equation (46) with respect to η from 0 to h_w and utilizing equation (63) yields:

$$\frac{dT_{1,c}(t)}{dt} = -\frac{h_w}{4k_{eff}}\frac{dq_{1,c}(t)}{dt} - \frac{2\alpha_{eff}}{k_{eff}h_w}q_{1,c}(t) + \frac{2\alpha_{eff}}{h_w^2}(T_{lv}(t) - T_{1,c}(t)). \quad (65)$$

Integrating the energy equation (45) with respect to η from h_w to $h_w + h_{wa}$ and utilizing equations (64) and (65) yields:

$$\frac{dq_{1,c}(t)}{dt} = \left\{ -\left(\frac{2Bi_{wa}(1+Bi_{wa})}{t_1} + \frac{Bi_w(3+Bi_{wa})}{t_2-t_1}\right)q_{1,c}(t) + \frac{2Bi_{wa}}{t_1}h_{conv}(T_{1,c}(t) - T_\infty) + \frac{3+Bi_{wa}}{t_2-t_1}h_{conv}(T_{lv}(t) - T_{1,c}(t))\right\} \Big/ (Bi_w(Bi_{wa}+3) + Bi_{wa}(Bi_{wa}+4)) \quad (66)$$

where $Bi_w = h_{conv}h_w/k_{eff}$. The temperature distributions are therefore given by equations (63)–(66). The heat flux at the liquid–vapor interface is:

$$q_{lv,c}(t) = \frac{2k_{eff}}{h_w}(T_{lv}(t) - T_{1,c}(t)) - q_{1,c}(t). \quad (67)$$

Vapor phase

The governing equations for the vapor phase are given in equations (4)–(7) for the disk-shaped heat pipe and equations (8)–(11) for the flat-plate heat pipe. The analytical solutions for the vapor phase are based on the works of Zhu and Vafai [19] for the disk-shaped heat pipe and Zhu and Vafai [16] for the flat-plate heat pipe. The vapor velocity profile and pressure distribution for the disk-shaped heat pipe are given as [19]:

$$u_v(r,y,\theta) = \begin{cases} 4U_v(r)\left\{a_3(r)\frac{y}{f} + \left(1-a_3(r)\frac{y}{f}\right) \times \left[2\frac{y}{f} - \left(\frac{y}{f}\right)^2\right]\right\}\frac{\theta}{\Phi}\left(1-\frac{\theta}{\Phi}\right) \\ (0 \leqslant y \leqslant f) \\ 4U_v(r)\left\{b_3(r)\frac{h_v-y}{h_v-f} + \left(1-b_3(r)\frac{h_v-y}{h_v-f}\right) \times \left[2\frac{h_v-y}{h_v-f} - \left(\frac{h_v-y}{h_v-f}\right)^2\right]\right\}\frac{\theta}{\Phi}\left(1-\frac{\theta}{\Phi}\right) \\ (f \leqslant y \leqslant h_v) \end{cases} \quad (68)$$

$$\frac{dp_v}{dr} = \frac{-4\rho_v}{1575h_v}\frac{d}{dr} \times \{r(U_v(r))^2[(2a_3^2(r) + 21a_3(r) + 112)f(r) + (2b_3^2(r) + 21b_3(r) + 112)(h_v - f(r))]\} - \frac{2\mu_v}{3h_v}\left(\frac{a_3(r)+2}{f(r)} + \frac{b_3(r)+2}{h_v - f(r)}\right)U_v(r) \quad (69)$$

and for the flat-plate heat pipe they are [16]

$$u_v(x,y,z) = \begin{cases} U_v(x)\left\{a_3(x)\frac{y}{f} + \left(1-a_3(x)\frac{y}{f}\right) \times \left[2\frac{y}{f} - \left(\frac{y}{f}\right)^2\right]\right\}\left(1 - a3\frac{z}{W/2}\right)^2 \\ (0 \leqslant y \leqslant f(x)) \\ U_v(x)\left\{b_3(x)\frac{h_v-y}{h_v-f} + \left(1-b_3(x)\frac{h_v-y}{h_v-f}\right) \times \left[2\frac{h_v-y}{h_v-f} - \left(\frac{h_v-y}{h_v-f}\right)^2\right]\right\}\left(1 - \left(\frac{z}{W/2}\right)^2\right) \\ (f(x) \leqslant y \leqslant h_v) \end{cases} \quad (70)$$

$$\frac{dp_v}{dx} = -\frac{8\rho_v}{15h_v}\frac{d}{dx}\{U_v(x)^2[(a_3^2(x)/105 + a_3(x)/10 + 8/15)f(x) + (b_3^2(x)/105 + b_3(x)/10 + 8/15)(h_v - f(x))]\} - \frac{2\mu_v}{3h_v}\left\{\left(\frac{a_3(x)+2}{f(x)} + \frac{b_3(x)+2}{h_v - f(x)}\right) + \left(\frac{W}{4h_v^2}\right)^2[(a_3(x)+8)f(x) + (b_3(x)+8)(h_v - f(x))]\right\}U_v(x) \quad (71)$$

where U_v denotes the maximum vapor velocity, f denotes the location of the maximum vapor velocity, a_3 and b_3 are coefficients used for the vapor velocity profile. The expressions in these quantities are given in [19] for the disk-shaped heat pipe and [16] for the flat-plate heat pipe. It should be noted that in both solutions, the vapor injection and suction velocities are time dependent in the present transient model and are obtained from equations (18)–(20).

The first-order ordinary differential equations for $T_{1,e}(t)$, $q_{1,e}(t)$, $T_{1,c}(t)$ and $q_{1,c}(e)$ are integrated numerically to obtain the temperature distributions within the heat pipe wall and wick regions. Since both the temperature and the heat flux at the liquid–vapor interface are unknown, a marching scheme in time is utilized. At each time step, a liquid–vapor interface temperature is assumed. The heat fluxes at the liquid–vapor interfaces are then calculated for both the evaporator section and the condenser section. A new liquid–vapor interface temperature is then obtained based on the energy balance for the vapor phase. The new liquid–vapor temperature is updated to calculate the new heat fluxes at the liquid–vapor interfaces

within the evaporator section and the condenser section. This iterative procedure continues until the liquid–vapor interface temperature converges. The fourth-order Runge–Kutta method is used to solve for the vapor velocity profiles and pressure distributions at each time step.

RESULTS AND DISCUSSION

The results based on the present analysis are obtained for a copper disk-shaped heat pipe and a copper square flat-plate heat pipe with heavy water as the working fluid. To make the comparison meaningful, the diameter of the disk-shaped heat pipe is taken equal to the length of the square flat-plate heat pipe, i.e., $R = L$. On the same basis, the heat input area, the heat pipe wall and wick thicknesses for both the disk-shaped and the square flat-plate heat pipes are taken to be equal. The respective dimensions of the heat pipes are chosen as: $R = L = 0.25$ m, $h_{wa} = 0.002$ m and $h_w = 0.003$ m. The radius of the circular heat input zone and the internal flow channel angle for the disk-shaped heat pipe are taken as 0.125 m and 45°, respectively. The width of the internal flow channel for the square flat-plate heat pipe is taken as 0.06 m. The vapor channel height is taken as 0.025 m. The top and bottom wick material is sintered copper powder, its effective pore radius, porosity and permeability are taken as 35.8 μm, 0.61, 4.25×10^{-11} m^2, respectively. The heat pipes are initially at room temperatures (296 K) when an input heat power of 25 kW is applied uniformly to the outer wall surface of the evaporator section at $t = 0$. The outer wall boundary condition at condenser sections is chosen as a convective boundary condition with the heat transfer coefficient of 1200 W m^{-2} K^{-1} and the coolant temperature of 296 K.

Figures 3 and 4 show the transient response of the power throughput and the temperatures for the disk-shaped heat pipe and the flat-plate heat pipe during the startup process, respectively. Our results show that the thermal layer takes a very short time (0.045 s) to reach the liquid–vapor interface because of the large thermal diffusivity of the copper wall and sintered copper wick. As shown in Figs. 3(a) and 4(a), the power throughput of the evaporator increases rapidly during the initial phase of the transient. Conversely, the power throughput of the condenser increases much slower and reaches the steady-state about 50 s later than that of the evaporator. This is because the thermal capacity of the evaporator is smaller than that of the condenser due to the fact that the condenser area is seven times larger than the evaporator area for the disk-shaped heat pipe and nine times for the flat-plate heat pipe. Before the heat pipe reaches steady state, there is a difference between the input power and the output power. This difference between the input and output powers is stored as sensible heat in the heat pipe wall and liquid–wick regions. The difference between the input power and the power throughput at the vapor–liquid interface represents the increase in the sensible heat of the evaporator, and the difference between the power throughput at the vapor–liquid interface and the output power represents the increase in the sensible heat of the condenser. As can be seen in Figs. 3(a) and 4(a), the increase in the sensible heat of the condenser is much larger than that of the evaporator.

The transient responses of the vapor temperature and the wall outer surface temperatures are shown in Fig. 3(b) for the disk-shaped heat pipe and Fig. 4(b) for the flat-plate heat pipe. Although the transient time for the power throughput of the evaporator is shorter, as shown in Figs. 3(a) and 4(a), the transient time for the evaporator wall outer surface temperature is the same as that of the vapor temperature and the condenser wall outer surface temperature. Since heat is conducted to the vapor–liquid interface through the heat pipe wall and liquid–wick in the evaporator section, the evaporator wall outer surface temperature is higher than the vapor temperature, while the vapor temperature is higher than the condenser wall outer surface temperature due to the fact that heat is conducted from the vapor–liquid interface to the condenser wall outer surface in the condenser section. This phenomena is also shown in Figs. 5–8. The temperature difference across evaporator wall and wick is larger than that across condenser wall and wick. This is because the heat flux in the evaporator is larger than that in the condenser due to the smaller evaporator area. During the initial phase of the startup transient, the temperature differences are small since a large part of the input power is stored as sensible heat in the heat pipe and the power throughput of the heat pipe is small. As time increases, the power throughput of the heat pipe increases, hence increasing the temperature differences across the heat pipe wall and wick. As the heat pipe approaches steady-state, the temperature differences reach their maxim.

The vapor and wall outer surface temperatures along the heat pipe at different times during the startup transient are shown in Fig. 5 for the disk-shaped heat pipe and Fig. 6 for the flat-plate heat pipe. For both disk-shaped and flat-plate heat pipes, the bottom wick acts as a condenser. Therefore, the temperatures at the bottom wall outer surface are almost uniform. This indicates that neglecting heat conduction along the heat pipe is reasonable for the bottom wall and wick regions. However, since the center part of the top wall and wick acts as the evaporator and the outside edge of the top wall and wick acts as the condenser, there is a temperature difference between the evaporator section and the condenser section within the top wall and wick regions. The assumption of neglecting heat conduction along the heat pipe may cause some error for the top wall and wick regions when input power is high. During both the transient and the steady-state, the temperature rise of the flat-plate heat pipe is always smaller than that

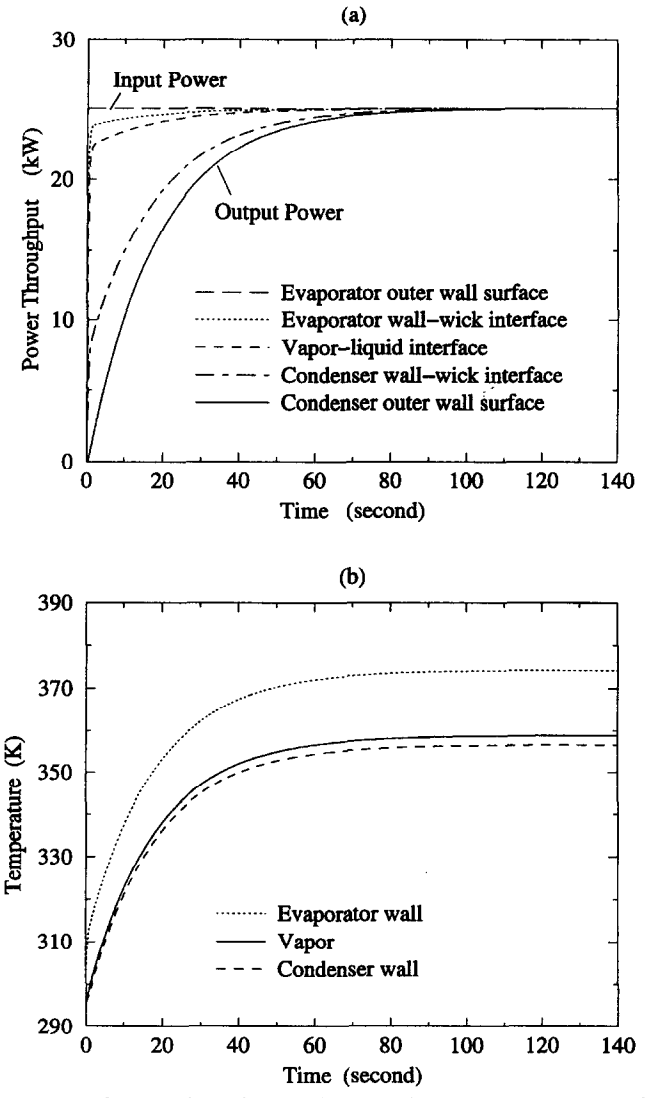

Fig. 4. Transient response of power throughput and temporal temperature response of the disk-shaped heat pipe.

of the disk-shaped heat pipe. This is because the square flat-plate heat pipe has a larger condenser area than the disk-shaped heat pipe, thus, dissipating more heat.

The heat pipe vertical temperature distribution at different times during the startup transient are shown in Fig. 7 for the disk-shaped heat pipe and Fig. 8 for the flat-plate heat pipe, where h_v represents the height of vapor space. In the $0 \leqslant r \leqslant R_e$ $(0 \leqslant x \leqslant L_e)$ region, the top wick acts as evaporator and the bottom wick acts as condenser. Therefore, the temperatures in the top wall and wick are higher than vapor temperature and the temperatures in the bottom wall and wick are lower than vapor temperature. In $R_e \leqslant r \leqslant R$ $(L_e \leqslant x \leqslant L)$ region, both top and bottom wicks act as condenser, therefore the temperature distribution is symmetrical due to the symmetrical cooling conditions. Since the effective thermal conductivity of the liquid-saturated wick is much smaller than that of the heat pipe wall, the temperature drops across the liquid–wick are much larger than that across the heat pipe wall.

The transient response of the maximum vapor velocity and the vapor pressure is shown in Figs. 9 and 10. The vapor pressure at the evaporator end, $r = 0$ $(x = 0)$, is taken to be zero in the analytical model [16, 19]. It can be seen that both the maximum vapor velocity and the vapor pressure drop increase with time. This is because the power transported by vapor phase from the evaporator section to the condenser section increases with time. It should be noted that the presented pressure distribution is the relative pressure

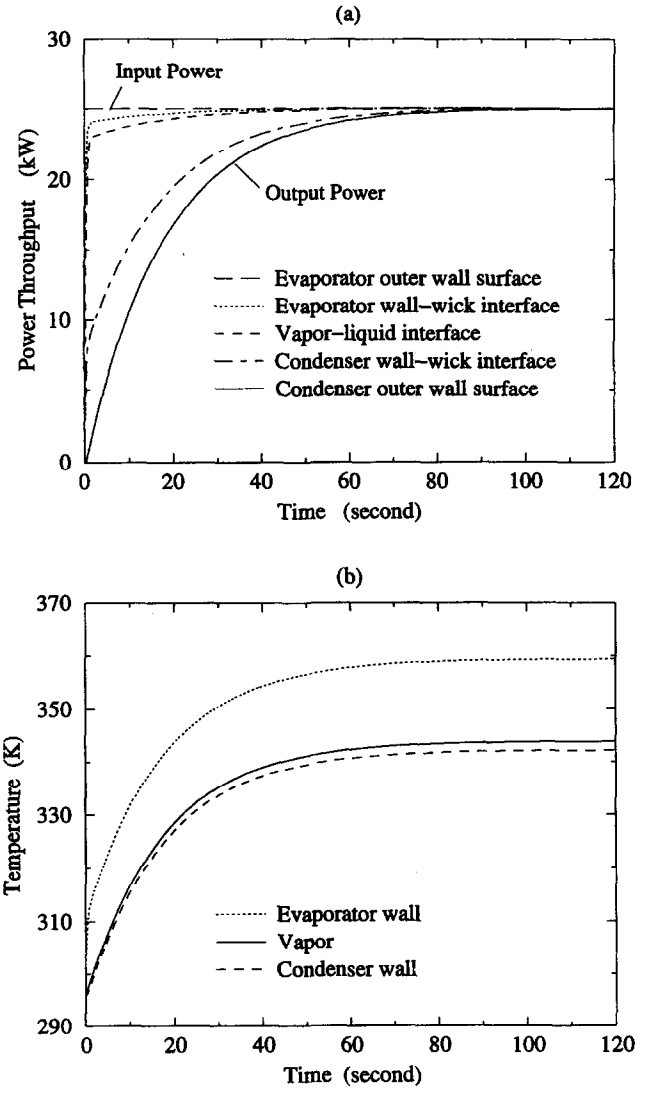

Fig. 5. Transient response of power throughput and temporal temperature response of the flat-plate heat pipe.

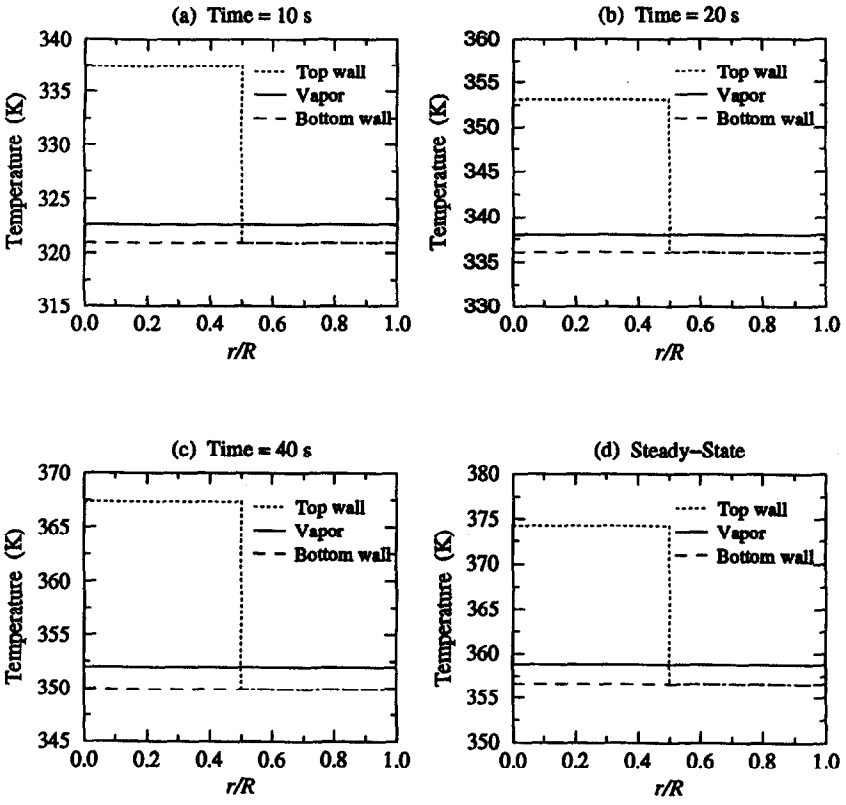

Fig. 6. Vapor and wall temperatures along the disk-shaped heat pipe at different times during the transient startup process.

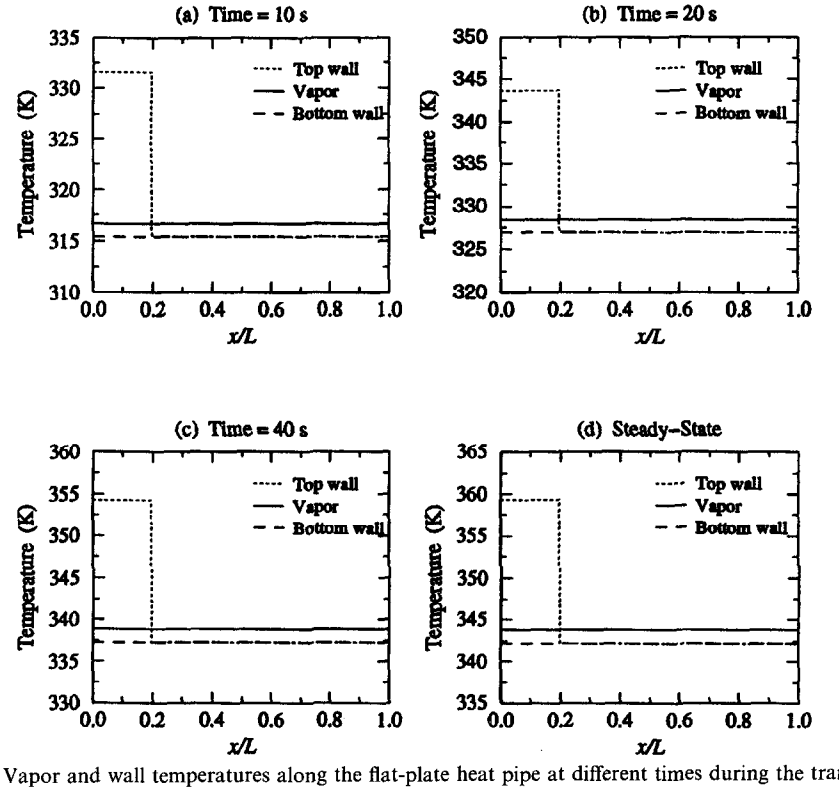

Fig. 7. Vapor and wall temperatures along the flat-plate heat pipe at different times during the transient startup process.

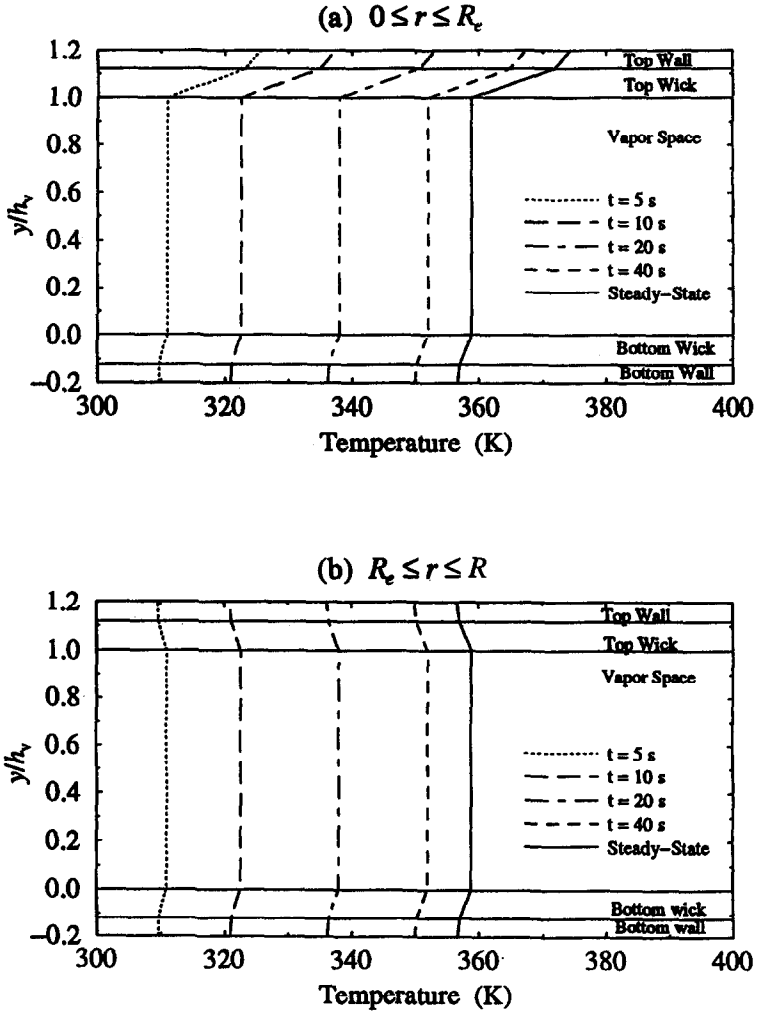

Fig. 8. Vertical temperature distributions of the disk-shaped heat pipe at different times during the transient startup process.

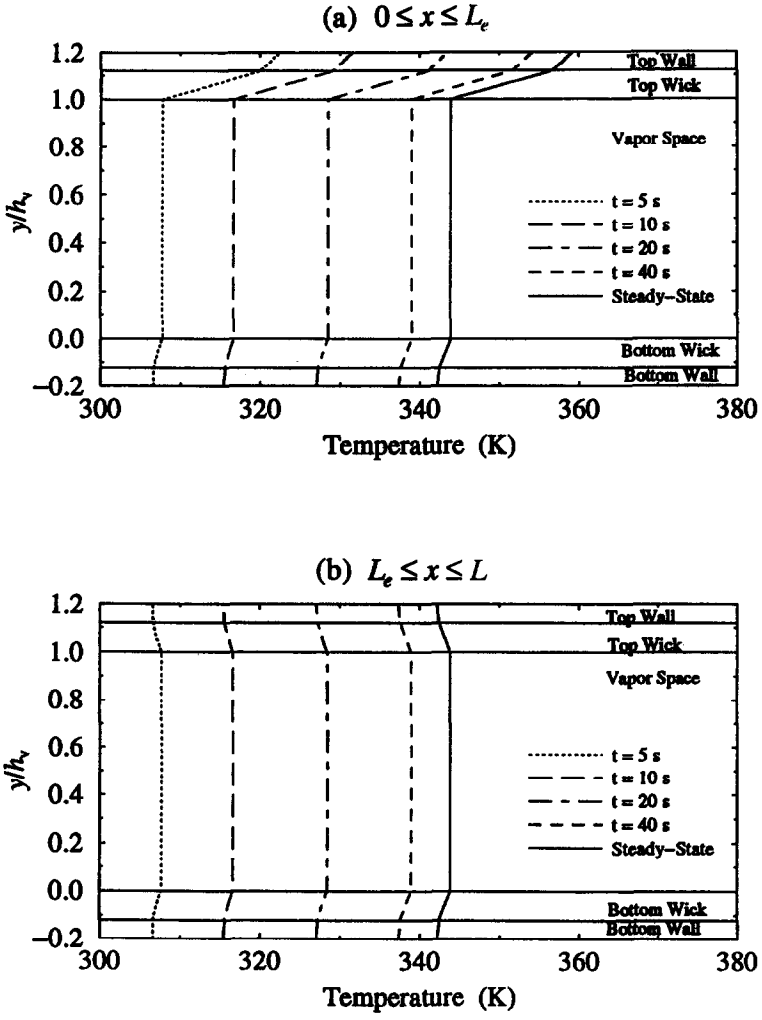

Fig. 9. Vertical temperature distributions of the flat-plate heat pipe at different times during the transient startup process.

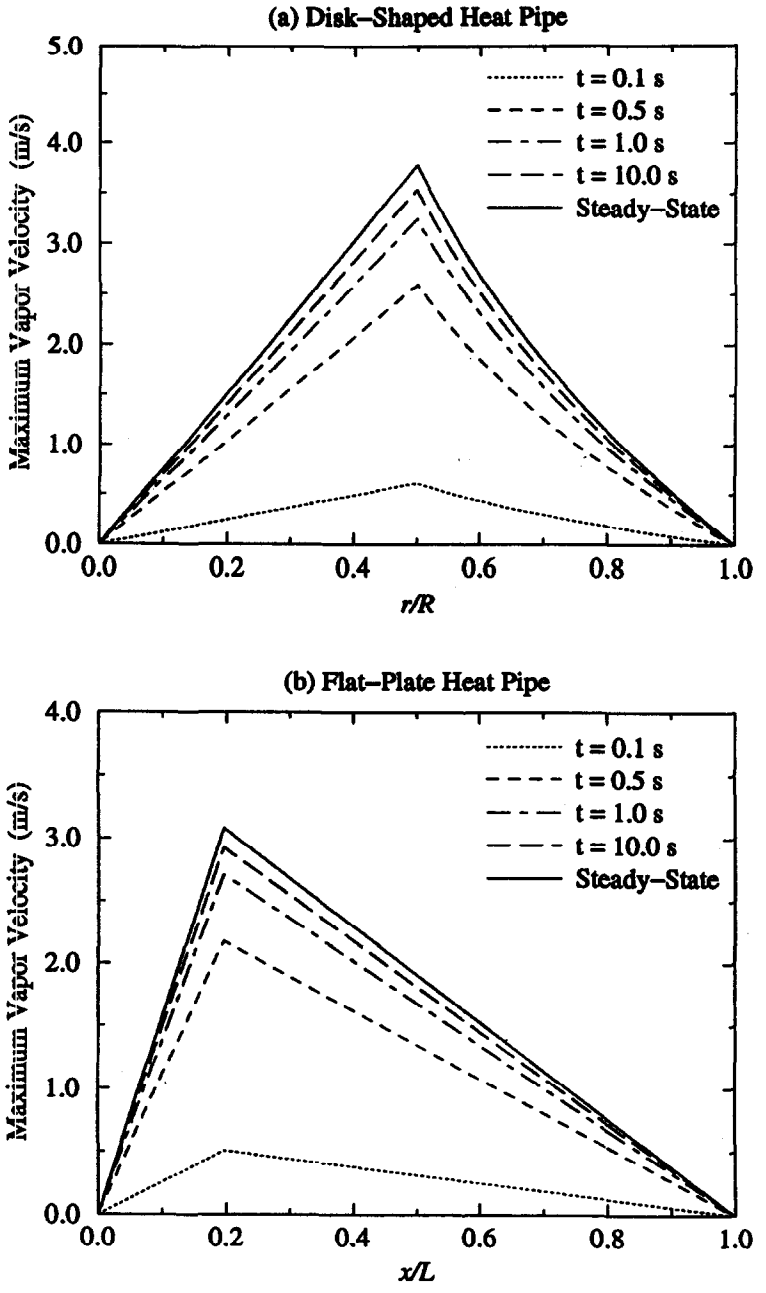

Fig. 10. The maximum vapor velocity along (a) the disk-shaped heat pipe and (b) the flat-plate heat pipe at different times during the transient startup process.

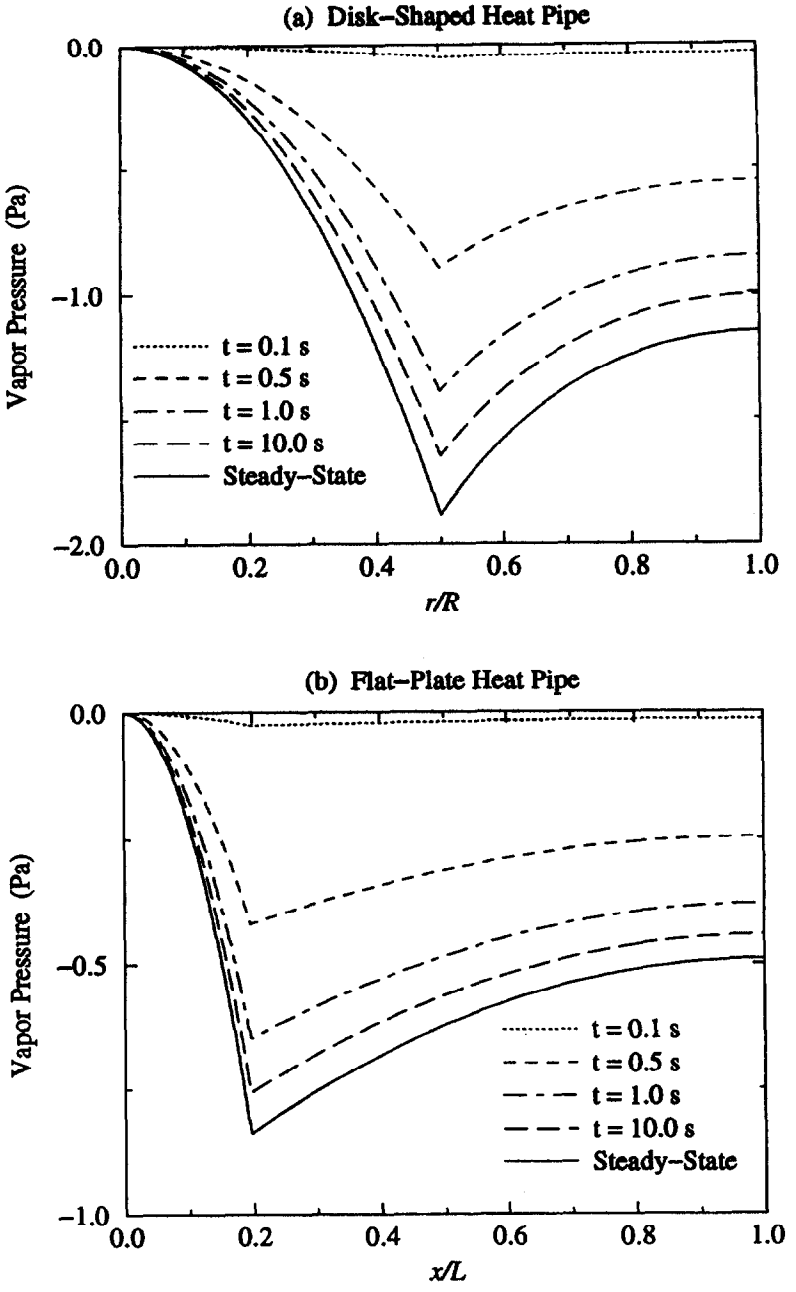

Fig. 11. Vapor pressure distribution along (a) the disk-shaped heat pipe and (b) the flat-plate heat pipe at different times during the transient startup process.

distribution. The absolute pressure distribution can be related to the vapor temperature at the evaporator end.

CONCLUSIONS

The startup operating characteristics of fully-thawed asymmetrical flat-plate and disk-shaped heat pipes has been analyzed in depth in this work. The transient heat transfer within the heat pipe wall and liquid-wick regions has been solved and is coupled to the vapor phase through energy balance of the vapor phase. A quasi-steady state, pseudo-three-dimensional analytical model is used for the flow and heat transfer in the vapor phase. Analytical results for a disk-shaped heavy water heat pipe and a square flat-plate heavy water heat pipe are presented. The results presented cover the entire startup transient of the heat pipes from the initiation of the startup to steady state.

Acknowledgement—The support by the Department of Energy under grant number DE-FG02-93ER61612 is acknowledged and appreciated.

REFERENCES

1. Ooijen, H. and Hoogendoorn, C. J., Vapor flow calculations in a flat-plate heat pipe. *AIAA Journal*, 1979, **17**, 1251–1259.
2. Thomson, M., Ruel, C. and Donato, M., Characterization of a flat plate heat pipe for electronic cooling in a space environment. *1989 National Heat Transfer Conference*. Philadelphia, Pennsylvania, 1989, **HTD-111**, 59–65.
3. Vafai, K. and Wang, W., Analysis of flow and heat transfer characteristics of an asymmetrical flat plate heat pipe. *International Journal of Heat and Mass Transfer*, 1992, **35**, 2087–2099.
4. North, M. T. and Avedisian, C. T., Heat pipe for cooling high flux/high power semiconductor chips. *Journal of Electronic Packaging*, 1993, **115**, 112–117.
5. Gerasimov, Yu. F., Dolgirev, Yu. E. and Gadelshin, M. Sh., Large-size flat heat pipes. *Heat Transfer Research*, 1993, **25**, 938–944.
6. Vafai, K., Zhu, N. and Wang, W., Analysis of asymmetrical disk-shaped and flat plate heat pipes. *ASME Journal of Heat Transfer*, 1995, **117**, 209–218.
7. Chang, W. S. and Colwell, G. T., Mathematical modeling of the transient operation characteristics of a low temperature heat pipe. *Numerical Heat Transfer*, 1985, **8**, 169–186.
8. Doster, J. M. and Hall, M. L., Numerical modeling of high-temperature liquid-metal heat pipes. *1989 Joint ASME/A.I.Ch.E. National Heat Transfer Conference*. Philadelphia, Pennsylvania, 1989, **89-HT-13**, 1–9.
9. Seo, J. T. and El-Genk, M. S., A transient model for liquid metal heat pipes. *Space Nuclear Power Systems*, 1988, ed. M. S. El-Genk and M. D. Hoover, **9**, 405–418.
10. Tournier, J.-M. and El-Genk, M. S., A heat pipe transient analysis model. *International Journal of Heat and Mass Transfer*, 1994, **37**, 753–762.
11. Sockol, P. M. and Forman, R., Re-examination of heat pipe startup. *Proceedings of the 9th IEEE Thermionic Conversion*, 1970, pp. 571–573.
12. Ochterbeck, J. M., Modeling of room-temperature heat pipe startup from the frozen state. *AIAA Journal of Thermophysics and Heat Transfer*, 1997, **11**, 165–172.
13. Bowman, W. J. and Hitchcock, J., A compressible vapor flux model for transient heat pipe analysis. *Transactions of the 4th Symposium on Space Nuclear Power Systems*, 1987, CONF-870102-Summs, pp. 358–388.
14. Merrigan, M. A., Keddy, E. S. and Sena, J. T., Transient performance investigation of a space power system heat pipe. *Proceedings of the AIAA/ASME 4th Joint Thermophysics and Heat Transfer Conference*, Boston, MA, 1986.
15. Zhu, N. and Vafai, K., The effects of liquid–vapor coupling and non-Darcian transport on asymmetrical disk-shaped heat pipes. *International Journal of Heat and Mass Transfer*, 1996, **39**, 2095–2113.
16. Zhu, N. and Vafai, K., Vapor and liquid flow in an asymmetrical flat plate heat pipe—a three-dimensional analytical and numerical investigation. *International Journal of Heat and Mass Transfer*, in press.
17. Tournier, J.-M., El-Genk, M. S. and Juhasz, A. J., Heat-pipe transient model for space applications. *Proceedings of the 8th Symposium on Space Nuclear Power Systems*, Albuquerque, NM, 1991, pp. 857–868.
18. Dunn, P. D. and Reay, D. A., *Heat Pipes*, 3rd edn. Pergamon Press, New York, 1982.
19. Zhu, N. and Vafai, K., Numerical and analytical investigation of vapor flow in a disk-shaped heat pipe incorporating secondary flows. *International Journal of Heat and Mass Transfer*, 1997, **40**, 2887–2900.
20. Özisik, M. N., *Boundary Value Problems of Heat Conduction*. International Textbook Company, Pennsylvania, 1968.